Measurement and Simulation of Topographic Effects on Passive Microwave Remote Sensing Over Mountain Areas: A Case Study From the Tibetan Plateau

Xinxin Li, *Member, IEEE*, Lixin Zhang, *Member, IEEE*, Lutz Weihermüller, Lingmei Jiang, *Associate Member, IEEE*, and Harry Vereecken, *Member, IEEE*

***Abstract*— Knowledge about the surface soil water content is essential because it controls the surface water dynamics and land–atmosphere interaction. In high mountain areas in particular, soil surface water content controls infiltration and flood events. Although satellite-derived surface soil moisture data from passive microwave sensors are readily available for most regions globally, mountainous areas are often excluded from these data (or at least flagged as biased) due to the strong topographic influence on the retrieved signal. Even though a substantial volume of literature is available dealing with topographic effects on spaceborne brightness temperature, no systematic analysis has been reported. Therefore, we present a comprehensive analysis of topographic effects on brightness temperature at C-band using a two-step approach. First, a well-controlled field experiment is carried out using a mobile truck-mounted C-band radiometer to analyze the impact of geometric and adjacent effects on the radiometer signal. Additionally, a comprehensive radiative transfer model is developed accounting for both effects and tested on the ground-based data. Second, recorded Advanced Microwave Scanning Radiometer–Earth Observing System (AMSR-E) data over the Tibetan Plateau were used to analyze the error due to the impact of topography using the developed model. The results of the field experiment clearly show that the geometric effect of a single hill has a much larger impact on brightness temperature compared to the adjacent effect of multiple hills, whereby, due to the geometric effect, the bias is up to +20 K for horizontal and −13 K for vertical polarization. For the adjacent effect, the bias is less than 3 K for both polarizations. Additionally, the developed radio transfer model was able to reproduce both effects with high accuracy. For the AMSR-E data, the model shows that the brightness temperature recorded is biased in the same way as the ground-based measurements and that uncertainties induced by the wide existence of atypical mountain regions in the Tibetan Plateau will have a great impact on the retrieving error (maximum 30%). The largest impact on the retrieval error, on the other hand, is calculated for the soil moisture with a maximum relative error of 44%. The negligible impact can be attributed to false parameterization of the soil texture, soil surface temperature, and sky temperature. Finally, the overall absolute error in the estimated water content is quantified on average with 4%, whereby single pixels indicate a maximum absolute error of up to 16%. In conclusion, we show that recorded spaceborne brightness temperatures are highly biased by topographic effects in mountainous regions using a comprehensive radiative transfer model. Additionally, we suggest using this model to invert the effective surface emissivity of mountain areas for standard processing of higher level data products such as surface soil water content.**

***Index Terms*— Advaned Microwave Scanning Radiometer–Earth Observing System (AMSR-E), mountain area, passive microwave remote sensing, radiometer, topography.**

I. Introduction

TERRESTRIAL surface water is one of the major components of the climate system because it controls the dynamics and thermodynamics of the atmosphere through the exchange of water and heat fluxes from the soil to the atmosphere [1], [2]. Especially, the soil water content is a key variable controlling mass and energy fluxes, and therefore, knowledge of the spatially distributed soil water status is essential for climatic prognoses. Additionally, knowledge of the surface soil water content is essential in a wide range of agricultural and hydrological research applications, as well. For example, surface soil moisture strongly controls the infiltration processes, but also raises the possibility of generating surface run-off in elevated terrains. Combining the water content information based on remote sensing data with land surface models (LSMs) as performed by [3] can potentially improve flood risk prediction and water management.

Spaceborne remote sensing, especially by passive microwave sensors such as the NASA's Advanced Microwave Scanning Radiometer–Earth Observing System (AMSR-E) or ESA's Soil Moisture and Ocean Salinity (SMOS) mission, provide integrated information on the surface soil moisture, which is valuable for mapping large areas [4]–[6]. Especially for remote areas or regions with limited access, remote sensing will be of great value. A large part of these regions are the mountain ridges which occupy one-quarter of the Earth's surface and provide resources and services for about one-fourth of the global population [7].

Manuscript received October 12, 2011; revised April 6, 2012, October 18, 2012, and February 14, 2013; accepted February 15, 2013. Date of publication April 18, 2013; date of current version December 12, 2013. This work was supported in part by the National Natural Science Foundation of China under Grant 41030534 and the National Basic Research Program of China under Grant 2013CB733406.

X. Li, L. Zhang, and L. Jiang are with the State Key Laboratory of Remote Sensing Science, Beijing Normal University and the Institute of Remote Sensing Applications of Chinese Academy of Sciences, Beijing 100875, China (e-mail: lixx213@mail.bnu.edu.cn; lxzhang@bnu.edu.cn; jiang@bnu.edu.cn).

L. Weihermüller and H. Vereecken are with Forschungszentrum Jülich GmbH, Jülich 52425, Germany (e-mail: l.Weihermuller@fz-juelich.de; h.vereecken@fz-juelich.de).

Color versions of one or more of the figures in this paper are available online at http://ieeexplore.ieee.org.

Digital Object Identifier 10.1109/TGRS.2013.2251887

It is known that soil moisture estimates based on satellite passive microwave remote sensing are greatly biased by topographic effects (e.g., [8]–[10]). The main influences on the upwelling brightness temperature (T_B) are the modification of the optical depth of the atmosphere, the radiometer observation angle which becomes a function of the surface slope, the shadowing of parts of the scene by mountains, the radiation reflected from one tilted surface to another, and finally, the depolarization effect [11].

For the optical wavelength range, radio transfer models accounting for topographic effects have already been developed since 1960 [12]–[14], and an overview of these works is presented in [15]. On the other hand, radio transfer modeling accounting for topographic effects at the microwave wavelengths started only two decades ago, among which [8] was the first to point out the influence of topography on radiation "relief effect." Based on this work, an increasing number of studies were devoted to relief effects for passive microwave remote sensing. In the beginning, empirical orthogonal functions (EOFs) were used to analyze the relationship between topography and soil moisture to be retrieved from passive microwave remotely sensed imagery [9]. It was shown that topography appeared to be the dominant factor for accurate soil moisture prediction only during and immediately after rainfall. The bias introduced by topography effects on brightness temperature can be more than 10 K compared to the reference flat terrain [10]. According to [8], the land surface scattering consists of two parts: 1) a specular part, and 2) Lambertian scattering. Based on the observed geometry and radiation transfer, the influence on altitude, slope, and shadowing was discussed in several studies.Topographic effects on the microwave radiation were analyzed for different frequencies ranging from X-band and C-band to L-band in other studies (e.g., [11], [16], [17]) by the use of forward ray-tracing techniques to account for the relief information taken from digital elevation maps (DEMs). The results show that the error in satellite microwave radiometric data is particularly correlated to the mean values of the height and slope within the radiometric pixel, as well as to the standard deviation of the aspect and local incidence angle. With respect to the spaceborne L-band radiometer missions SMOS, [18] analyzed the influence of topography on the upwelling T_B by means of a distributed ecohydrology model in combination with a radiative transfer model at the hillslope scale. They proved that the tens of meter scale influences microwave radiation in the same way as the kilometer scale. Unfortunately, all these studies were only used in forward mode to estimate the topographic effects, but were not used to retrieve the actual surface T_B for the mountainous area from real observation data.

Additionally, different attempts were made to flag pixels or sensor footprints where the topography is substantially biasing the calculated surface T_B [10], [19], [20]. In this case, the analysis was based directly on the statistics of the DEM, which is highly computationally demanding. As an alternative, [20] replaced the full information of the DEM with a probability density function (pdf) for slopes. Next, they separated the pdf into "smooth" and "rough" distributions, which provided insight into situations where the topography would become important to the observed signal. However, their studies only accounted for topographic effects on land emission, without incorporating scattered radiation or shadowing effects into their approaches.

Meanwhile, ground-based experiments have been gradually conducted for L-band to analyze the effect of small-scale topography on the recorded signal [21]. In [22], different scenarios were analyzed, namely vegetated and non-vegetated, as well as flat and nonflat terrains, with the results indicating that topography seem to have the largest impact if the soil was bare.

In conclusion, most studies dealing with topography effects relay on topographic geometry information only (e.g., slope, angle, and aspect), but the topographic ruggedness, which is another significant topographic character, describing the complexity of terrain using roughness parameters (e.g., standard deviation of elevation, and elevation correlation length) and affecting surface diffuse scattering of mountain areas, has not been considered until now, resulting in a deviation of observed from the "real" brightness temperatures over mountain areas.

With respect to this problem, we analyzed the topographic effect from two different points of view in our study. First, we performed a well-controlled field experiment using artificially constructed hills observed by a truck-mounted C-band radiometer; then we exploited AMSR-E data recorded over the Tibetan Plateau. Both datasets were compared to an improved simple radiative transfer model to calculate the "real" brightness temperature, which is based on the geometric optics approximation [20] for microwave land emission, surface scattering, and shadowing effects. The advantage of the proposed model lies in its simplicity, and, therefore, can be easily implemented into standard data processing algorithms for higher level data processing. Besides the observation geometry, a set of roughness parameters was introduced to describe the effect of terrain complexity on land emission and scattering at hill scales. Finally, the soil surface moisture content was estimated based on the model results for a test area within the Tibetan Plateau.

II. Experiments

A. Ground-Based Experimental Setup

To study the effects of topography on the microwave emission recorded by the Truck-Mounted Multifrequency Microwave Radiometer (TMMR) operating at C-band, a synthetically hilly landscape was constructed in 2009 and 2010 at the field test site of Baoding (Hebei) in the North of China. The material for construction was taken off the site and can be characterized as a fluvio-aquic soil (calcariccambisol, FAO) [23] with a sand, silt, and clay content of 51.7, 40.1, and 8.2 mass%, respectively. Care was taken in order that the size of the designed landscape appropriately matched the footprint of the radiometer at C-band, and that the hills were fully covered by the footprints at different angles. Following these prerequisites, the constructed conical hills were 1.5 m in diameter and ranged in heights between 0 to 0.75 m. In order to avoid the measured brightness temperatures being affected

Fig. 1. Two constructed conical hills perpendicular to the radiometer (slope angle of 40°) within the 4 m^2 footprint of the TMMR. The visible footprint for TMMR is 1.5×1.5 m covered by one hill (left), and the other hill (right) stands out of the view to observe the adjacent effect on the visual field.

by radiance originating from areas outside the conical hills, the flat surface was covered by aluminum sheets before construction (Fig. 1). Based on this general setup, aspects and slopes of the artificial surface were varied from 0° to 360° and 0° to 40°, respectively.

Additionally, the ground-based microwave radiometer was used to measure different hill combinations: 1) single hill; 2) two hills in a row perpendicular to the radiometer; 3) two hills in a row both parallel and perpendicular to the track carrying the radiometer (see Fig. 1); or 4) three hills within a triangle. This setup allowed not only observing different slope and aspect combinations of any individual conical hill as the primary relief effect, namely the observation geometry effect, but also the effect of multiple-hills within a landscape, namely the adjacent or secondary effect.

B. Ground-Based Measurements

All measurements were performed by the TMMR designed by Radiometer Physics GmbH (Meckenheim, Germany) and Beijing Normal University, China. The nonimaging TMMR operates in five channels centered at 6.925, 10.65, 18.7, 36.5, and 89 GHz at both vertical and horizontal polarization. It consists of four components: the antennas, the positioner, the host software, and the platform. It is to be noted that only the first channel has been used for this study. The microwave emission of the scene collected by the antenna is first split into vertical and horizontal polarization components using an orthomode transducer. In a next step, the signal is amplified by a 40-dB low-noise amplifier (LNA) and filtered by waveguide band-pass filters before it is amplified by another 20-dB LNA. Finally, the detected signal is processed and stored in a computer. The 6.925-GHz antenna is characterized by a sidelobe level lower than −30 dB, a directivity of 28.3 dB, and a half-power beamwidth (HPBW) of 6.85. Before the experiment, the instrument calibration was carried out by the four-point calibration procedure proposed in [25]. An overview of the TMMR specifications is given in Table I.

TABLE I
TECHNICAL SPECIFICATIONS OF THE TMMR MICROWAVE RADIOMETER SYSTEM

Items	Performances
System noise temperature	< 500 K
Radiometric resolution	0.5 K
Receiver and antenna thermal stability	< 0.05 K
Antenna sidelobe level	< −30 dB
Radiation measurement range	0–350 K
Operating temperature	−30–45 °C
Antenna azimuth range observed	0°–360°
Antenna pitch angle range of observation	−90° to + 90°
The largest increase in height of the antenna	8.2 m
System peak power	<3 kW
Power supply system	5 kW

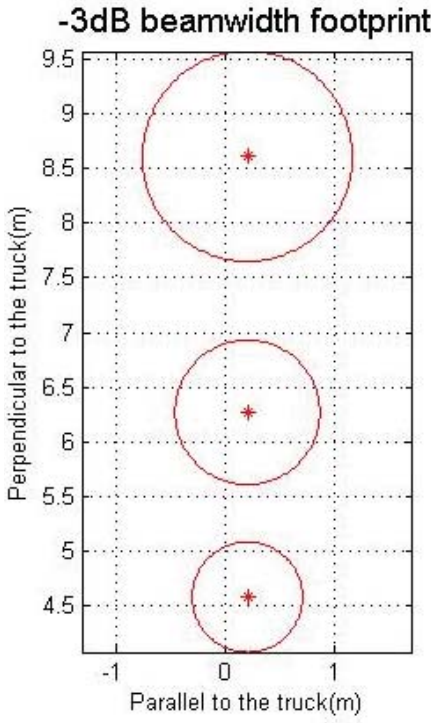

Fig. 2. Radiometer (SMMR) observation footprint with −3 dB beam width.

Effects of topography on microwave brightness temperature measured at C-band can be divided into the observation geometry effect, which modulates the microwave emission, and the adjacent effect modulating the microwave radiation scattered by the surrounding elevated terrain. These two effects can be measured separately by the controlled experimental setup, which extends to the maximum target footprint (2×2 m), determined by the circle approximation of the antenna half-power beamwidth, as shown in Fig. 2. The three circles in Fig. 2 along the y-axis from 4.5 to 9.5 m represent three observed radiometer angles (10°, 30°, and 55°), respectively. By moving the truck and adjusting the truck position, the radiometer can observe the entire topographic landscape adequately. Additionally, soil moisture and soil temperature were kept constant over the measurements period

(soil moisture = 0.128 cm^3 cm^{-3}, and soil temperature = 15.8 °C). To measure the observation geometry effect, the single conical hill was built up with slopes ranging from 0° to 40°. After the radiometer measurements, the land surface temperature was recorded by using an infrared temperature sensor, and undisturbed soil samples were extracted to measure the volumetric soil moisture. In general, brightness temperature was first recorded over the flat terrain, and then a conical hill with a slope of 40° was constructed. This measurement protocol was repeated for slopes of 30°, 20°, and 10°, respectively. Besides the measurements of single hills, multiple hill scenes were constructed with identical slope angle (40°) to analyze the effect of adjacent objects. Here, the observation started from two hills in a row perpendicular to the truck carrying the radiometer (Fig. 1). Then radiation from a couple of hills placed parallel to the truck was also collected. In general, only one hill was within the radiometer footprint, but the scattering from the other hill into the radiometer footprint was also taken into account in this experimental setup. This stepwise approach allowed us to perform a detailed analysis of the effect of increasing terrain complexity on the emission from the same footprint, and the contribution from adjacent elements. For a better overview of the experimental procedure, the flow chart as depicted in Fig. 3 describes the entire process.

C. AMSR-E Experiment Dataset

To test the reliability of the radiative transfer model described in Section III, data recorded by the AMSR-E were used. AMSR-E is a microwave radiometer operating on the NASA's polar-orbiting Aqua satellite platform and measures vertically (v) and horizontally (h) polarized brightness temperatures at six frequencies (6.9, 10.7, 18.7, 23.8, 36.5, and 89.0 GHz) at a constant Earth observation angle of 55° from nadir. In this paper, we use the AMSR-E L2A brightness temperatures acquired at 6.925 GHz over the Tibetan Plateau on August 1 and 2, 2008, between 6:00 and 8:00 (UTC). The AMSR-E data were processed according to two steps: 1) invalid data with zero values were filtered out, and 2) data indicating radio frequency interference (RFI) were removed by using frequency and polarization thresholds as suggested by [26] and [27].

D. AMSR-E Experiment Input Data

In order to compare measurements with the radiative transfer simulations, it is needed to set a number of soil parameters including sand, silt, and clay content (mass%), soil bulk density (g cm^{-3}), and volumetric soil moisture content (cm^3 cm^{-3}). The soil textural parameters were provided by the digital soil map of the Food and Agriculture Organization of the United Nations (FAO-UN) with a spatial resolution of 5×5 arc-min for a depth of 0 to 4 cm [28]. The volumetric soil moisture data were obtained from AMSR-E L3 soil moisture product, and the topographic information was extracted from the digital elevation model (DEM) originated from NASA's shuttle radar topography mission (SRTM) [30], with a resolution of 1 km. From the DEM data, slopes, aspects, local zenith angles of the terrain, and the complexity of topography

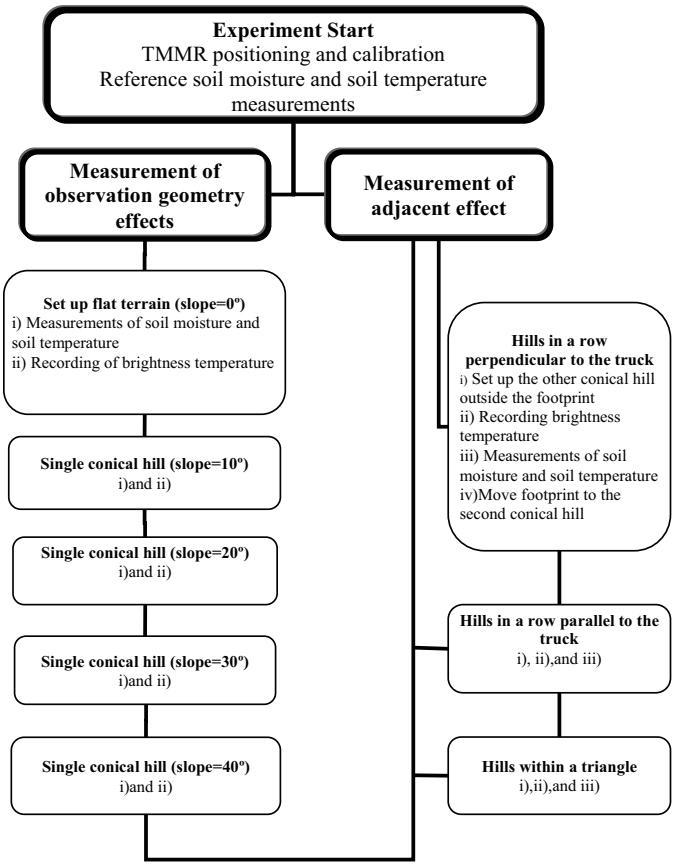

Fig. 3. Overview of the measurement protocol for the relief effect experiment.

were computed. Soil surface temperature was extracted from the global land data assimilation system (GLDAS) data of the Noah land surface model (LSM) [29] for a soil depth of 0 to 4 cm. Soil temperature is assumed to decrease with increasing altitude according to the standard temperature gradient of 6.5 K km^{-1} [17]. GLDAS soil moisture in a layer of 0–4 cm depth was also used for analyzing the error of the AMSR-E soil moisture data. It is to be noted that the soil temperature was kept constant over the soil depth (0–4 cm), which corresponds to the maximum penetration depth of the considered frequency, and that freezing and thawing cannot be handled by the model.

To reduce the confounding effect of vegetation on the brightness temperature, two sub-study areas were selected. The first one was selected based on the land surface classification standards of the International Geosphere Biosphere Program (IGBP) [31] with predominantly bare soil pixels; the second one was characterized by low values of normalized differential vegetation index (NDVI) (less than 0.3) taken from 16 days observation of NASA's Moderate-resolution Imaging Spectroradiometer (MODIS) during the same time interval.

III. Radiative Transfer Model

A. Relief Effects on Microwave Radiation

In general, mountainous landscapes influence the brightness temperature (T_B) recorded by any spaceborne microwave sensor. These so-called relief effects [8] can be described by geometrical properties and the complexity of terrain within

the observed scene. The topographic geometrical properties are generally described by the slope angle, aspect, altitude, and zenith angle of the terrain.

First, elevation determines the path of the microwave radiation through the atmosphere, and therefore the atmospheric emission and attenuation, but at C-band this effect can be neglected [8]. Additionally, soil temperature decreases with elevation according to a standard temperature gradient of 6.5 K km^{-1} [17]; thus, elevation can diminish land emission in mountainous areas.

Second, the slope and aspect are critical features, describing the orientation of each surface facet, and thus affecting the polarization seen from the surface with respect to that referred to the satellite reference frame. Reflection and emission from a tilted surface facet in the global coordinate frame (i.e., satellite–Earth surface) can be expressed as function of the reflection and emission in the local coordinate frame (surface facet) and the slope angle a (°) and azimuth angle β (°) of the facet. The transformation from the global to the local plane of incidence affects both the polarization and scattering geometry. As proposed by [8], the local angle of incidence θ_l can be calculated from global incidence angle θ by

$$\cos(\theta_l) = \cos\alpha \bullet \cos\theta + \sin\alpha \bullet \sin\theta \bullet \cos\beta \tag{1}$$

where the resulting quantity will be positive for all visible surface facets. Furthermore, ϕ is defined as the azimuth angle of the satellite, and the linear polarization is rotated by an angle φ, given by

$$\sin\varphi = \sin(\phi - \beta)\sin\alpha / \sin\theta_l. \tag{2}$$

The local emissivity E_v and E_h along the observation direction θ_l defined in the local reference frame can be represented in the global (satellite–Earth surface) reference system as a function of the global observation direction θ, taking into account the polarization rotation as in [8]

$$E_v(\theta) = E_v(\theta_l)\cos^2\varphi + E_h(\theta_l)\sin^2\varphi \tag{3}$$

$$E_h(\theta) = E_v(\theta_l)\sin^2\varphi + E_h(\theta_l)\cos^2\varphi. \tag{4}$$

In mountainous areas, the microwave signal of one mountain also includes the radiation scattered from its surrounding elevated terrains, resulting in an enhancement of microwave radiation, named the "adjacent effect." To calculate the adjacent effect, the zenith angle of the terrain (θ_H) is introduced. θ_H is defined as the zenith angle of incidence from the surrounding elevated terrain. For a given point in a horizontal profile through a landscape (Fig. 4), θ_H is the zenith angle (measured with respect to the global vertical direction) under which the elevated terrain is observed [8], and also the lowest zenith angle at which the sky radiation can be observed, which can be calculated by

$$\cot\theta_H = \frac{h_B - h_C}{x_C - x_B} \tag{5}$$

$$\cot\theta_H = \frac{h_O - h_A}{x_O - x} \tag{6}$$

$$\cot\theta_H = \frac{h_O - h_A}{x_O - x_A} \tag{7}$$

$$\cot\theta_H = 0. \tag{8}$$

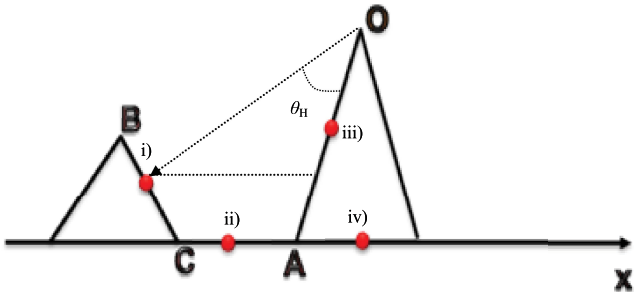

Fig. 4. Supplying solutions for the zenith angle of terrain θ_H with sub-four cases.

For further understanding, let us consider a horizontal profile in a certain direction x through a landscape, as shown in Fig. 4. The radiation is scattered from an elevated terrain where the gray point moves along between the two endpoints. At various position x (x_B, x_C, x_A, x_O), the computation of θ_H is accomplished by inverting the cotangentcot θ_H. 1) If $x_B < x < x_C$, then θ_H is given by (5); 2) if $x_C < x < x_A$, then θ_H is given by (6); 3) if $x_A < x < x_O$, then θ_H is given by (7); and 4) if $x > x_O$, then θ_H is given by (8).

Relief effects can also be expressed as function of the complexity of the terrain besides the topographic geometrical properties, which in turn is related to topographic roughness parameters that can be derived from a DEM. Essentially, topography can be treated as large-scale roughness at the scale of several tens of kilometers to more than 100 km [20], whereby the complexity of terrain can be parameterized by roughness parameters [32] such as the standard deviation of elevation S and elevation correlation length cl. At the coarse resolution of microwave radiometer pixels (e.g., 25×25 km), these parameters are computed locally within a moving window scanning the DEM. $Z(x_i)$ is the height value of the ith element of the DEM (e.g., 1×1 km), and is the average height within the moving window. N is the number of DEM elements in the moving window [32]. Finally, S can be computed by

$$S = \sqrt{\frac{\sum_{i=1}^{N}[Z(x_i) - \overline{Z}]^2}{N-1}}. \tag{9}$$

The correlation length cl is calculated from the autocorrelation function of the surface height using also DEM data. The height autocorrelation function estimated within the moving window is therefore

$$\rho_i(k) = \frac{\sum_{i=1}^{N-k-1}\{[Z(x_i) - \bar{Z}] \cdot [Z(x_{i+k}) - \bar{Z}]\}}{\sum_{i=1}^{N-1}[Z(x_i) - \overline{Z}]^2} \tag{10}$$

where the kth element of this array contains the autocorrelation computed at lag k, where $k = 1, \ldots, N$. In our analysis, N was set to the maximum lag value of 25 considering the resolution of 1 km of the DEM. Thus, the correlation length of surface elevation within a microwave pixel (cl) is

$$cl = h \cdot \Delta x \tag{11}$$

where h is equal to k when $\rho(k) = e^{-1}$, e is the Euler number equal to 2.71828, and Δx is the DEM spatial resolution [m]. The ratio of S/cl, defined as the relief gradient, is the

first derivative of the function representing the terrain surface height, and denotes the rate of variability of elevation with distance. The variability of the relief gradient and the second derivative of the terrain surface function provide information about the concave–convex features of the topography. Finally, the relief gradient defines the topographic roughness at the macroscopic scale corresponding to spaceborne microwave resolution.

B. Microwave Radiative Transfer

In mountainous areas, different components of the microwave radiation have to be accounted for to correct data collected from spaceborne radiometers such as AMSR-E. Primarily, the p-polarized emitted brightness temperature, $T_{p\mathrm{em}}$, of the hemispherical half-space with its emissivity $E_{\mathrm{p}}(\theta_{\mathrm{l}})$ is given by

$$T_{p\mathrm{em}} = E_{\mathrm{p}}(\theta_{\mathrm{l}}) \cdot T_{\mathrm{S}}(z) \tag{12}$$

where T_s (K) is the physical soil temperature of a certain DEM element at height z [m]. Note that the land emission $E_{\mathrm{p}}(\theta_{\mathrm{l}})$ (i.e., $[1 - R_{\mathrm{p}}(\theta_{\mathrm{l}})]$, R_{p} being the soil reflectivity) will be determined by the local incident angle (θ_{l}) as shown in (3) and (4), and calculated by (18) and (19) in the local frame.

Secondly, the radiation scattered by the land surface ($T_{p\mathrm{sc}}$) has to be taken into account. Thereby, the radiation can be generalized to include radiation impinging from all observed directions and scattered in the observed direction. Underlying the soil bistatic scattering coefficient, the reflectivity R_{p} at polarization $p = h$ and υ in (14) will be composed of a specular polarized component $R_{\mathrm{p}}^{\mathrm{sp}}$ and of a diffuse unpolarized component $R_{\mathrm{p}}^{\mathrm{in}}$. To compute all multiple reflections and emissions from the elevated landscape, [11] proposed the following equations:

$$\begin{aligned} T_{p\mathrm{sc}} = {} & \upsilon R_{\mathrm{p}}^{\mathrm{sp}} T_{\mathrm{sp}} + (1-\upsilon)(R_{\mathrm{p}}^{\mathrm{in}}/\pi) \\ & \cdot \left[\int_{\Delta\Omega_{\mathrm{ground}}} T_{B_{\mathrm{groud}}}(\theta_{\mathrm{H}}, \varphi_{\mathrm{H}}, z) \cdot \cos\theta_{\mathrm{H}}\, d\Omega_{\mathrm{H}} \right. \\ & \left. + \int_{\Delta\Omega_{\mathrm{sky}}} T_{B_{\mathrm{sky}}}(\theta_{\mathrm{H}}, z) \cdot \cos\theta_{\mathrm{H}}\, d\Omega_{\mathrm{H}} \right] \end{aligned} \tag{13}$$

$$R_{\mathrm{p}} = \upsilon R_{\mathrm{p}}^{\mathrm{sp}} + (1-\upsilon) R_{\mathrm{p}}^{\mathrm{in}} \tag{14}$$

where υ spans the interval [0, 1], representing the specular factor, T_{sp} is the brightness temperature coming from the specular direction being coherently reflected, whereas T_{Bground} is the downwelling T_{B} coming from below the horizon. Φ_{H} denotes the azimuth angle corresponding to the horizon, and $\Delta\Omega_{\mathrm{ground}}$ is the solid angle under which each individual facet observes the surrounding terrain, with $\Delta\Omega_{\mathrm{sky}}$ as the corresponding quantity for the sky radiation.

However, [8] simplified the computation of $T_{p\mathrm{sc}}$ by assuming that the elevated surface is a black body at constant temperature, whereas the lower surface is a rough surface (not a black body) at the same physical temperature, and that the sky brightness temperature can be neglected. Additionally, they assumed a constant value of $\cos\theta_{\mathrm{H}}$ for all interacting surface elements. Finally, the simplification leads to

$$\begin{aligned} T_{p\mathrm{sc}} &= (1 - R_{\mathrm{p}}^{\mathrm{in}}) \cdot T_{\mathrm{S}} \cdot [1 + cR_{\mathrm{p}}^{\mathrm{in}} + (cR_{\mathrm{p}}^{\mathrm{in}})^2 + (cR_{\mathrm{p}}^{\mathrm{in}})^3 + \cdot] \\ &= T_{\mathrm{S}} \frac{1 - R_{\mathrm{p}}^{\mathrm{in}}}{1 - cR_{\mathrm{p}}^{\mathrm{in}}} \end{aligned} \tag{15}$$

where indicates the mean value. Furthermore, assuming the specularly reflected component radiated from the sky, $T_{p\mathrm{sc}}$ can be expressed by

$$T_{p\mathrm{sc}} = (1 - R_{\mathrm{eff}}) T_{\mathrm{s}} + R_{\mathrm{eff}} \cdot T_{\mathrm{sky}} \tag{16}$$

and the effective reflectivity R_{eff} can now be evaluated from

$$R_{\mathrm{eff}} = R_{\mathrm{p}}(\theta_{\mathrm{l}}) \cdot \frac{1 - c}{1 - cR_{\mathrm{p}}(\theta_{\mathrm{l}})}. \tag{17}$$

Replacing $R_{\mathrm{p}}(\theta_{\mathrm{l}})$ by $[1 - E_{\mathrm{p}}(\theta_{\mathrm{l}})]$ yields the effective emissivity and can be used for soil moisture retrieval in mountainous areas (Section V) can be computed by (14) and the following equations:

$$R_{\mathrm{p}} = Q_{\mathrm{p}} \cdot R_q^{\mathrm{sp}} + (1 - Q_{\mathrm{p}}) \cdot R_{\mathrm{p}}^{\mathrm{sp}} \tag{18}$$

$$\log\left[Q_{\mathrm{p}}(f)\right] = a_{\mathrm{p}}(f) + b_{\mathrm{p}}(f) \cdot \log(S/cl) + c_{\mathrm{p}}(f) \cdot (S/cl) \tag{19}$$

where Q_{p} is the roughness parameter of the land surface, a_{p}, b_{p}, and c_{p} are experimental parameters for the different polarizations, is the Fresnel reflectivity at polarization $p = h$ or υ, and is at polarization $q = \upsilon$ or h. In general, the incoherently scattered radiance is independent of the scattering direction, which is in good agreement with the trend of the bistatic scattering coefficient for a given incident angle which was assessed by the well-established advanced integral equation model (AIEM) of [34] as shown in (18) and (19).

In conclusion, microwave radiative transfer over mountainous areas can be expressed by

$$T_{\mathrm{B}p} = T_{p\mathrm{em}} \cdot t + T_{p\mathrm{sc}} \cdot t + T_a \cdot (1 - t). \tag{20}$$

The third and the fourth term in (20) refer to the radiative effective temperature of the atmosphere (weighted-average temperature profile) T_a, which can be neglected if the frequency is less than 10 GHz, and $1 - t$ is the atmosphere emissivity.

Consequently, as mentioned in Section III-A, the contribution of some surface facets may be enhanced or reduced depending on the observation direction, or may even be hidden for given observation directions, depending on the incidence angle, slope, and orientation of every facet of the DEM. As a result, the total signal at a given polarization T_{p} collected by the radiometer (such as AMSR-E) is a beam-weighted sum over the radiation from all facets $T_{\mathrm{B}p}$ (numbered from $i = 1$ to N) within the antenna footprint

$$T_p = \frac{\sum_{i=1}^{N} T_{Bpi} \frac{\cos\theta_{\mathrm{l}i}}{\cos\alpha_i}}{\sum_{i=1}^{N} \frac{\cos\theta_{\mathrm{l}i}}{\cos\alpha_i}}. \tag{21}$$

Here, the local incident angle is set to θ_{l}, α refers to the slope angle, and the brightness temperature $T_{\mathrm{B}pi}$ from each DEM element can be computed by (20). To derive integrated T_{p} from input land surface parameters at different spatial

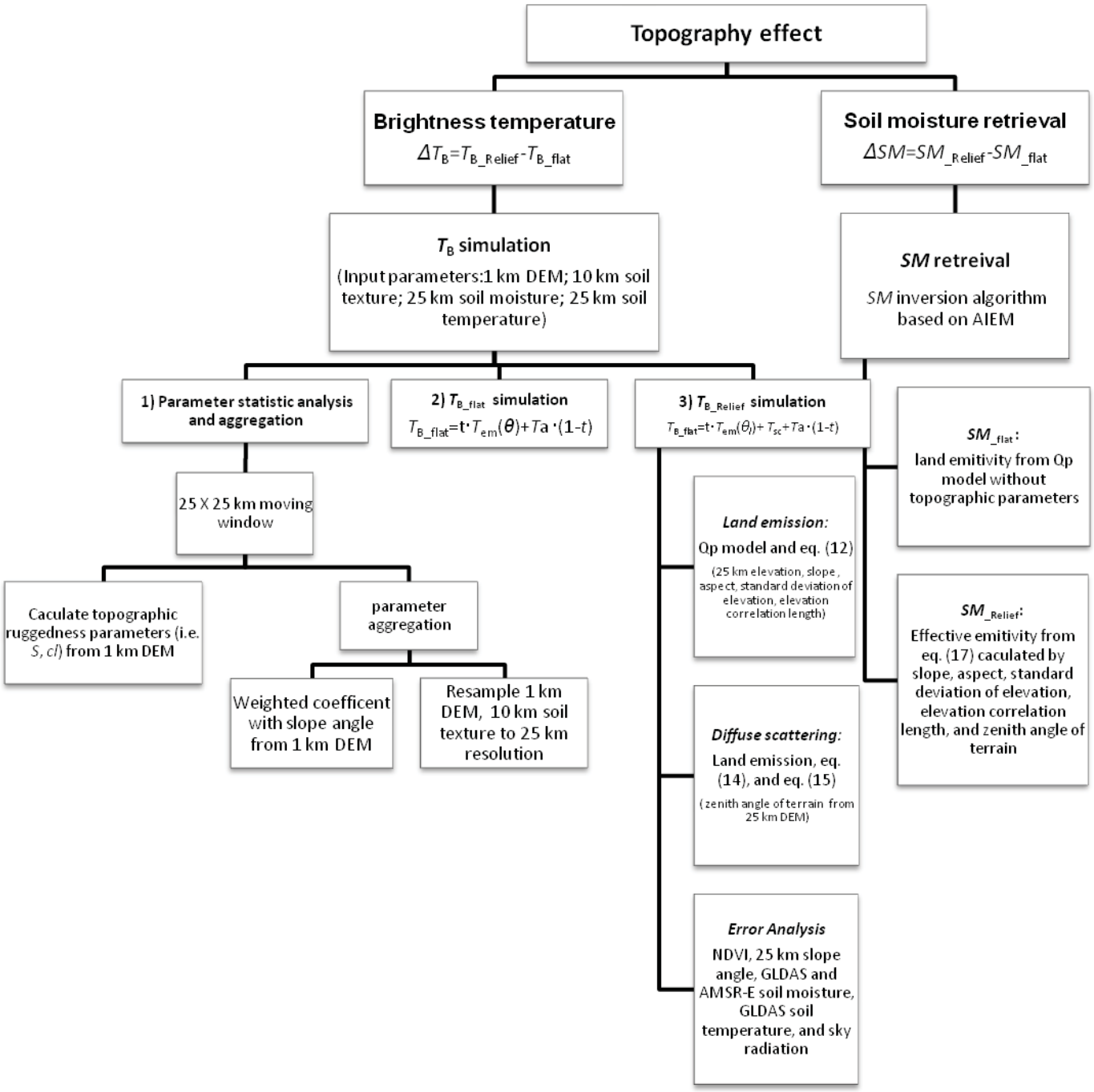

Fig. 5. Overview of relief effect estimation at satellite-observed scale.

resolutions, the weighting coefficient () was calculated from DEM, and the input parameters with higher resolution than 25 km were resampled (e.g., DEM data and soil texture data of FAO-UN). In the last step, T_{Bpi} was substituted by using the beam-weighted sum in (21). Finally, all the input data at the same radiometric scale were involved to simulate T_B and, consequently, T_p was obtained. To be explicit, Fig. 5 exhibits an overview of the topography effect estimation on microwave radiation and soil moisture inversion at the space borne radiometric scale.

IV. Results and Discussion

A. Experimental Results

In a first step, we analyzed the brightness temperatures T_B recorded by the C-band TMMR over the different artificial hills. For the analysis of the geometry effects, the difference in brightness temperature (T_{B_DIFF}) was calculated between the brightness temperatures recorded for each scene (T_{B_HILL}) with respect to the reference brightness temperature measured over the flat terrain (T_{B_FLAT}). Correspondingly, the adjacent

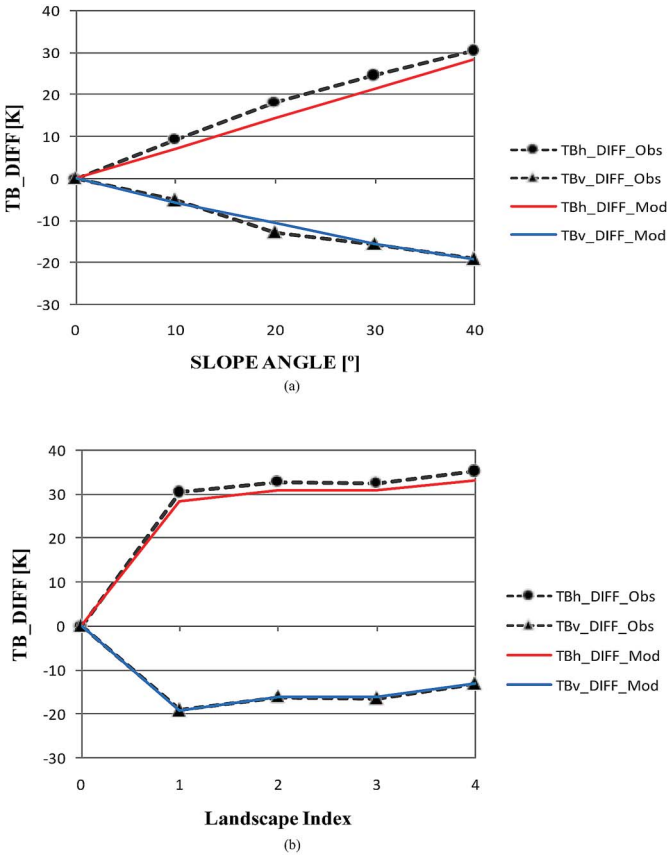

Fig. 6. Comparison of experimental measurements and simulation results. (a) Observed geometry effect ($T_{B\_DIFF} = T_{B\_HILL} - T_{B\_FLAT}$) on single hills with different slopes (10° to 40°) at horizontal (T_{Bh_DIFF}) and vertical (T_{Bv_DIFF}) polarization. (b) Observation of the adjacent effect ($T_{B\_DIFF} = T_{B\_MULT} - T_{B\_SINGLE}$) over various terrain scenes ranging from flat terrain (landscape index = 0), single hill (landscape index = 1), hills in a row perpendicular to the radiometer (landscape index = 2), hills in a row parallel to the radiometer (landscape index = 3), and hills within a triangle (landscape index = 4) for horizontal (T_{Bh_DIFF}) and vertical (T_{Bv_DIFF}) polarization.The slope angle for all hills was 40°.

effect (T_{B_DIFF}) was computed as the difference between the brightness temperatures recorded over multiple hills (T_{B_MULT}) and the brightness temperature measured over a single hill (T_{B_SINGLE}).

Fig. 6(a) shows the computed geometry effects (T_{B_DIFF}) for single hills with different slope angles of 10°, 20°, 30°, and 40°, respectively. For horizontal polarization, the positive value of T_{B_DIFF} demonstrates that the geometry effect enhances the measured brightness temperature, whereby this effect increases nearly linearly with increasing slope angle, reaching a maximum of +30 K for a slope angle of 40°. On the other hand, brightness temperature diminishes at vertical polarization according to the negative T_{B_DIFF}, whereby the decrease is less (−20 K) compared to the enhancement at horizontal polarization. Because of the alteration of the observed angle and the occurrence of polarization rotation, the two polarized brightness temperatures are perturbed in opposite directions.

We have analyzed the adjacent effect in Fig. 6(b) for various terrain complexities ranging from flat terrain (landscape index = 0), single hill (landscape index = 1), hills in a row perpendicular to the radiometer (landscape index = 2), hills in a row parallel to the radiometer (landscape index = 3), and hills within a triangle (landscape index = 4). Note that the slope angle of each single hill was kept constant at 40°.

As can be seen in Fig. 6(b), T_{B_DIFF} largely increases when observing a single hill, as could be expected from the geometry effect. Additionally, the adjacent effect, which occurs only for terrain complexity with a landscape index larger than 2 (i.e., when at least two hills are present) contributes to a relatively small extent to the T_{B_DIFF} at horizontal polarization, with a maximum of +5 K for the landscape index 4 (hills within a triangle). The graph also shows a kind of saturation with increasing terrain complexity. For vertical polarization, T_{B_DIFF} is less sensitive to the increasing complexity, resulting in a difference in T_{B_DIFF} of +3 K at v polarization and +2.4 K at h polarization between the single hill and the most complex system of hills with the triangular arrangement. Finally, we have calculated the average ΔT_B for the observation geometry and the adjacent effect for all slope angles and complexities at both polarizations. The results are summarized in Table II. Again, it is clear that the impact of topography on the radiation from a single hill and the multiple hill scenario is different. Therefore, we classified the relief effects into a primary effect caused by varying slope and aspect angles, and a smaller secondary effect caused by adjacent hill elements.

Furthermore, we have computed the brightness temperature based on (20) for the known hill configurations and plotted the results also in Fig. 6. For the geometry or primary effect at horizontal polarization, a more or less linear increase can be observed, which corresponds fairly well with the observations [$R^2 = 0.99$, root mean square error (RMSE) = 1.3 K]. For the vertical polarized brightness temperature, a linear decrease was observed, which fits the measured data even better ($R^2 = 0.99$, RMSE = 1.0 K). For the adjacent or secondary effect [Fig. 6(b)], the correlation between simulated and measured T_{B_DIFF} is also high ($R^2 = 0.99$, RMSE = 0.17 K at v polarization and 0.79 K at h polarization), whereby the saturation effect was also well reproduced.

B. Brightness Temperature Simulation

Encouraged by the positive results from the modeling exercise of the field experiment, the brightness temperatures (T_B) over the Tibetan Plateau were simulated by the same microwave radiative transfer model accounting for the primary and secondary effects. We first identified all open water and glacier bodies within the observation pixels using the FAO-UN soil property and IGBP land cover maps available for the Tibetan Plateau [23]. Then, all these invalid pixels at the resolution of the radiometer (25 × 25 km) were denoted as *NaN* (not a number) to exclude them from further analysis. Additionally, all pixels with NDVI value larger than 0.3 were excluded. This resulted in the exclusion of 8.4% of pixels of water bodies and glaciers, 13.5% of pixels with NDVI exceeding 0.3, and 60% of pixels outside the region of the Tibetan Plateau. The simulated brightness temperatures are displayed for the entire Tibetan Plateau in Fig. 7(a) and (b) for the vertical and horizontal polarization, respectively.

In general, the topography of the Tibetan Plateau is characterized by higher mountains in the northwest and lower ones

TABLE II
OBSERVED AVERAGE ΔT_B FOR THE TWO DIFFERENT RELIEF EFFECTS

Relief Effects	ΔT_{Bh}	ΔT_{Bv}
The observation geometry effect → The primary effect	20.65 K	−13.26 K
The adjacent effect → The secondary effect	2.4 K	3 K

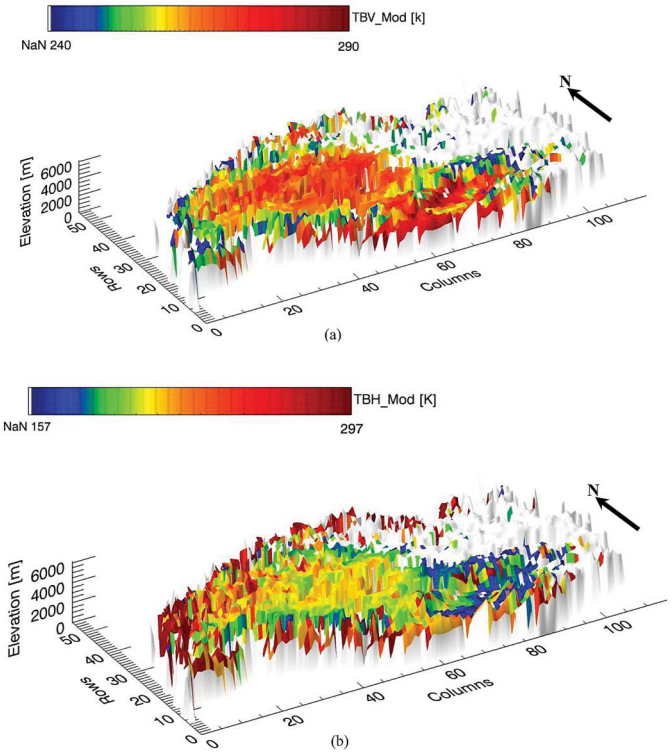

Fig. 7. Simulated brightness temperature at C-band for (a) vertical polarization and (b) horizontal polarization for the Tibetan Plateau.

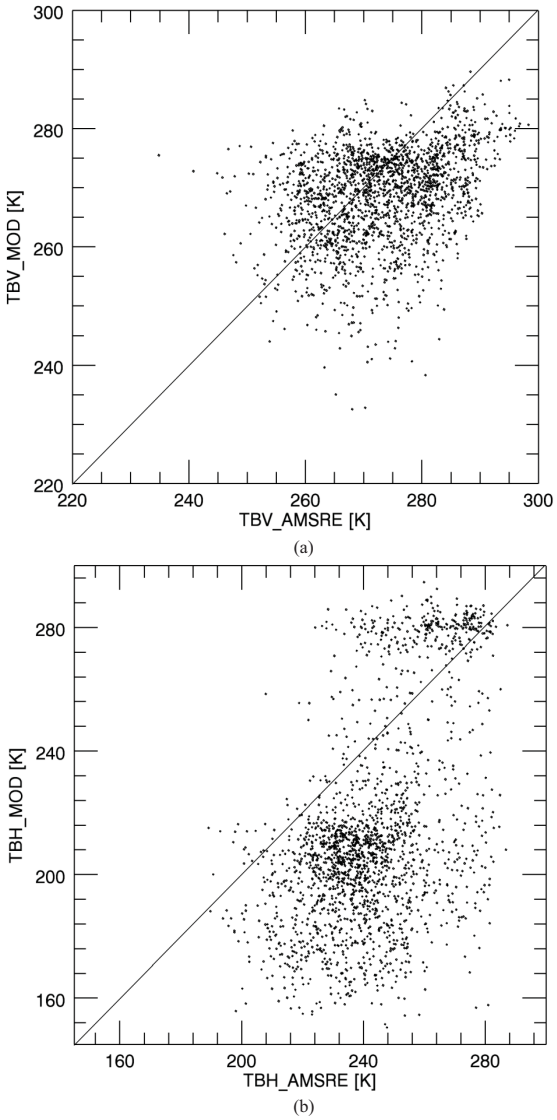

Fig. 8. Pixel-wise simulated T_{B_MOD} versus AMSR-E derived T_{B_AMSRE} brightness temperatures for (a) vertical polarization with 2074 pixels in total ($R^2 = 0.39$, RMSE = 11 K) and (b) horizontal polarization with 1984 pixels in total ($R^2 = 0.56$, RMSE = 25 K).

in the southeast. Additionally, the south and north edge of the plateau are much rougher than the hinterland, and the vast endothecia lakes are located in the northeast. The T_B simulation as depicted in Fig. 7 exhibits a spatial pattern that is inversed between polarizations. As shown in Fig. 7, the southward T_B at vertical polarization is brighter than T_B in the northern part, with most of the low T_B values are located toward the north. However, for horizontal polarization the T_B distribution is reversed, with higher T_B values in the northern plateau and lower values toward the south.

A pixel-wise comparison of the modeled and measured T_B's was carried out for the entire study area (2074 valid pixels in total) and plotted in Fig. 8 for both polarizations. In general, the agreement between the simulated T_B and AMSR-E observations across the entire study area, in terms of RMSE, is better at v polarization than h polarization. However, h-polarized T_B performs better than v-polarized T_B when we look at the correlation coefficient (R^2). The disagreement of simulated versus observed T_B (low RMSE) at h polarization is due to the large sensitivity of h polarization to spatial heterogeneity compared to v polarization. We attribute this larger sensitivity, for instance, to the impact of vegetation and topographic ruggedness. The poor correlation results for both polarizations between modeled and measured T_B, which leads to a maximum difference of 50 K, can be largely attributed either to random errors (i.e., those related to the input data) as well as intrinsic errors in the simulation. Next, we performed a statistical analysis of the deviations between T_{B_AMSRE} and T_{B_MOD} to evaluate various error contributions. There by, it was found that the deviation of the actual land cover type from input maps might be prone to errors. As stated above, all areas

TABLE III
ESTIMATION OF THE ERROR DISTRIBUTION BETWEEN AMSR-E MEASURED T_B AND SIMULATED T_B PIXEL BY PIXEL

Error Sources	Maximum Relative Error (%)	Maximum Absolute Error (K)
Vegetation	16	8
Flat terrain	30	15
Soil moisture	44	22
Soil temperature	4	2
Sky radiation	4	2
Soil texture parameters	2	1

were treated as bare soil even though a NDVI threshold of 0.3 was assumed. Additionally, approximately 60% of the area of the Tibetan Plateau is nearly flat without apparent topographic features, and only 40% of the entire plateau shows typical mountainous features. For example, only 20% of Tibetan Plateau has slope angles larger than 25° [24]. Therefore, large areas of the flat terrain with no significant topographic characters, such as a slope angle less than 10° and a zenith angle less than 10°, are prone to reveal more uncertainty of the vegetation and the roughness less than the microwave length in the T_B simulation. Besides the above considerations, the AMSR-E L3 soil moisture product, which was used in the forward simulation of the brightness temperature over the entire region, might be already biased by relief effects. Small errors can be also introduced by wrong parameterization of the physical soil temperature, which was provided by the GLDAS model, and the approximate estimation for the sky radiation. Finally, a random error component might be introduced by wrong soil texture parameters. Table III lists the various error contributions and their impact on brightness temperatures. The relative error is calculated by where i represents each individual error relative to the total bias between the simulated T_B and the observed T_B. The absolute error is derived directly by the T_B difference.

From Table III, it can be clearly seen that the largest error is related to the soil moisture parameterization, with a maximum relative error of 44% and a minimum relative error of 30%. A lower impact on the total error can be attributed to the widespread flat terrain in the area and to the wrong description of the vegetation cover, with a maximum relative error of 30% and 16%, respectively. The minor contribution to the overall error is expected from the uncertainty in soil temperature and sky radiation, with a maximum relative error of 4% only.

For a better understanding of the model results with respect to AMSR-E brightness temperatures (T_B), a subset of T_B from 17 pixels was arbitrary selected from bare soil locations according to the land surface classification and slope angle larger than 20°. Fig. 9(a) shows the comparison between the modeled and measured T_B's for the v polarization which led to a correlation coefficient (R^2) of 0.99 and an RMSE of only 0.8 K. Additionally, the same is plotted in Fig. 9(b) for the h polarization with an R^2 of 0.99, and an RMSE of 0.6 K. From these selected data, it turns out that the simulated T_B matches the AMSR-E observations fairly well. Therefore, it is convincing that our microwave radiative transfer model is suitable for simulating the brightness temperatures especially over strong topography and sparse vegetation as typically observed in high-altitude mountainous areas if an error-free input can be assumed.

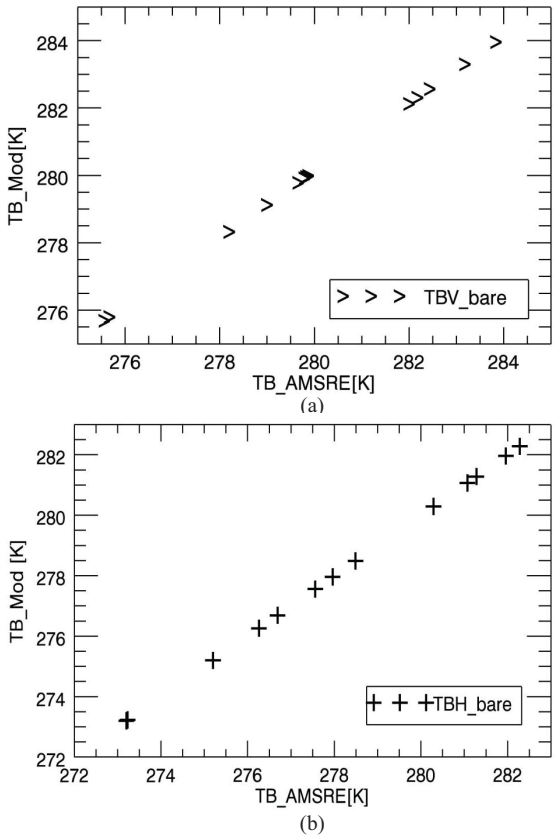

Fig. 9. Comparison between selected simulated and AMSR-E measured brightness temperatures (T_B) over uncovered pixels with slopes > 20° for (a) vertical (R^2 = 0.99, RMSE = 0.8 K) and (b) horizontal polarization (R^2 = 0.99, RMSE = 0.6 K).

C. Relief Effects on Microwave Radiation and Soil Moisture Retrieval

Finally, we evaluated the relief effects of the entire region based on the simulated brightness temperature difference (ΔT_B) between the brightness temperature of the mountainous areas (T_{B_relief}) and that of a reference flat terrain T_{B_flat}, where $\Delta T_B = T_{B\_relief} - T_{B\_flat}$. Again, only pixels where the NDVI is less than 0.3 and without any open water or glacier bodies were analyzed. Fig. 10(a) and (b) shows the calculated brightness temperature differences (ΔT_B) for the vertical and horizontal polarization, respectively. From the plot it can be clearly seen that for the v polarization the microwave radiation is largely attenuated by relief effects with $\Delta T_{Bv} < 0$. This effect covers 96% of the entire study area. On the other hand, h-polarized microwave radiation is enhanced ($\Delta T_{Bh} > 0$) for 97% of the study area. Generally, nearly 18 K bias was produced by relief effects in the intensely rough terrain, which is consistent with the results from the experimental measurement (i.e., about 20 K T_B errors).

Once computed, the brightness temperature difference introduced by the topography and the consequent systematic errors on the soil moisture retrieval should be assessed. To estimate

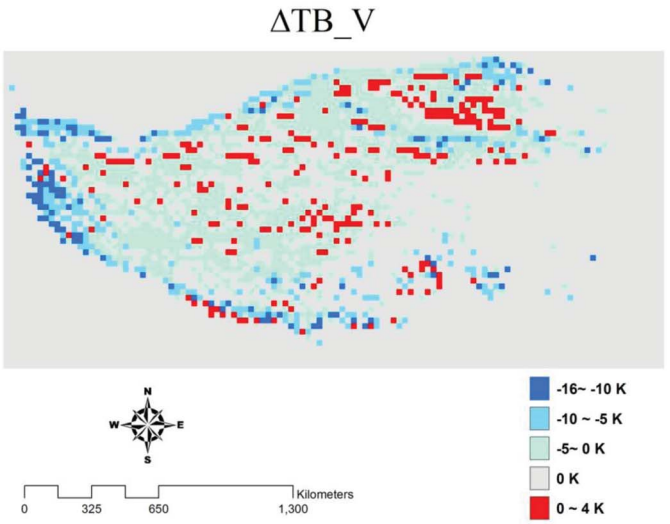

Fig. 10. Brightness temperature difference ΔT_B between T_{B_relief} and the flat reference T_{B_flat} for (a) vertical polarization and (b) horizontal polarization clustered to 5 levels.

the relief effects on soil moisture, the effective surface emissivity has been calculated based on the simulated T_B both considering the topography and assuming a flat terrain. Then, the soil moisture was retrieved from the effective surface emissivity simulated in both cases using Shi's inversion algorithm [34]. Finally, the systematic error of the retrieval was computed as the soil moisture difference (ΔMv) between that retrieved over the mountain area (Mv_{relief}) and that retrieved over a flat terrain (Mv_{flat}). The retrieval approach is a physically based bare-surface soil moisture inversion model developed for AMSR-E and using both polarizations at C-band [33] ($\Delta Mv = Mv_{relief} - Mv_{flat}$). Fig. 11 shows the soil moisture retrieval difference over the entire Tibetan Plateau and its surrounding areas. From the figure, we can clearly see that relief effects lead to an overestimation of soil moisture when relief effects are not considered. As expected, the largest errors are associated with regions with strong topographic features

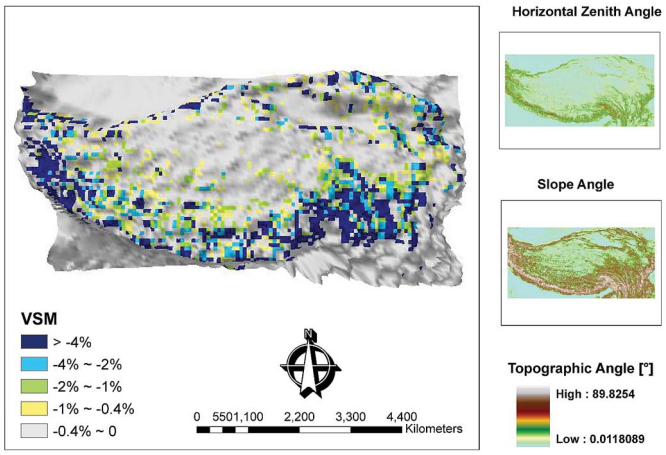

Fig. 11. Soil moisture difference ($M_{v\_relief} - M_{v\_flat}$) over Tibetan Plateau in volume % (VSM) with additional information about horizontal zenith angle, and slope angles computed from DEM.

(high terrain zenith and slope angles). Overall, the error in soil moisture retrieval is more than 4% in most locations, and the maximum error is even up to 16%, and, therefore, beyond the maximum allowed retrieval error [35]. It can be concluded that our modeling approach is feasible to correct the relief effects for accurate soil moisture retrieval.

V. Conclusion

In this paper, we presented a comprehensive but simple simulation approach accounting for relief effects due to topographic geometrical properties (i.e., slope and aspect angles), as well as the effect of adjacent elevated elements on radiometer measurements at C-band. In a first step, a field experiment was performed on different artificial hills varying in slope angle as well as spatial arrangement to analyze the radiometer signature collected by a TMMR operating at C-band. The results show that the geometry or primary effect is much larger (nearly by a factor of 10) than the adjacent or secondary effect. Additionally, the secondary effect seems to saturate for increasing complexity of the topography. The field experiment was also used to validate the developed model, whereby the simulated brightness temperatures showed good agreement with the measured ones. Encouraged by the positive results of the model applied to the well-controlled field experiment, the model was also applied to an area within the Tibetan Plateau which is characterized by high altitude, rough surface, and low vegetation. All topographic parameters were extracted from a DEM, whereas the vegetation was characterized using the IGBP land surface classification and NDVI. Additionally, soil physical temperature was taken from GLDAS model runs.

By comparing the simulated and AMSR-E brightness temperatures, it became clear that those areas with the largest topographic features show the largest mismatch between the model and the measured brightness temperatures. Analysis of the pixel-wise correlation between the modeled and measured data indicated the general consistency, whereby still some unexpected mismatches were detectable, which were related to the assumption of bare soil for the entire region (NDVI < 0.3), the impact of the widespread flat terrain, uncertainties

in the soil textural classification, uncertainties in GLDAS soil physical temperature, and sky radiation. Especially, uncertainties in soil moisture parameters involved in the model, which arise from relief effects on AMSR-E L3 soil moisture product, showed the largest impact on the brightness temperature simulation errors. Nevertheless, good agreement with an R^2 value of 0.99 could be achieved by comparing pixels where the soil was actually bare and the slope angle was $>20°$. By analyzing the spatial mismatch between the modeled T_B, considering relief effects and the reference T_B on flat terrain without consideration of relief effects, it was shown that the largest mismatch occurs over the strongly rough areas in the southern mountain belt of the Tibetan Plateau, which clearly confirms that brightness temperatures observed by spaceborne sensors are highly contaminated by relief effects. Furthermore, it was also shown that, within the 25×25 km AMSR-E footprint, the classically derived soil water content (AMSR-E L3 product) will not capture the mountain hydrological system accurately. This was shown by the fact that more than 96% of all pixels showed a clear overestimation of the AMSR-E L3 soil water content for both polarizations when relief effects were not considered on the mountainous areas. Therefore, topographic correction for spaceborne passive C-band is mandatory for a reliable land surface parameter retrieval, such as soil moisture, snow water equivalent, and phase transition of water in frozen soil over mountainous areas. Finally, we suggest using the proposed model for routinely post processing the C-band remote-sensed brightness temperature and deriving surface effective emissivity of mountain areas to increase the overall soil moisture retrieval by 4%–10%.

ACKNOWLEDGMENT

The authors would like to thank the Agrosphere Institute (IBG-3), Forschungszentrum Jülich GmbH, for supporting this work. The AMSR-E TB data and MODIS land cover in EASE grid format were provided by the National Snow and Ice Data Center (NSIDC). The soil texture data including soil sand content, clay content, and soil bulk density were provided by the Food and Agriculture Organization of the United Nations (FAO-UN). The land surface temperature was provided by the Global Land Data Assimilation System (GLDAS). This work was performed at the State Key Laboratory of Remote Sensing Science, Beijing Normal University.

REFERENCES

[1] C. M. Beljaars, P. Viterbo, M. Miller, and A. Betts, "The anomalous rainfall over United States during 1993: Sensitivity to land surface parameterization and soil moisture anomalies," *Mon. Weather Res.*, vol. 124, no. 3, pp. 362–383, 1996.

[2] Y. Liou and A. England, "A land surface process/radio brightness model with coupled heat and moisture transport for freezing soils," *IEEE Trans. Geosci. Remote Sens.*, vol. 36, no. 2, pp. 669–677, Mar. 1998.

[3] M. Rasmy, T. Koike, S. Boussetta, H. Lu, and X. Li, "Development of satellite land data assimilation system coupled with mesoscale model in the Tibetan Plateau," *IEEE Trans. Geosci. Remote Sens.*, vol. 49, no. 8, pp. 2847–2863, Aug. 2011.

[4] H. Vereecken, J. A. Huisman, H. Bogena, J. Vanderborght, J. A. Vrugt, and J. W. Hopmans, "On the value of soil moisture measurements in vadose zone hydrology: A review," *Water Resouces Res.*, vol. 44, no. 4, pp. 1–21, Apr. 2008.

[5] T. J. Jackson, J. Schmugge, and E. T. Engman, "Remote sensing applications to hydrology: Soil moisture," *Hydrol. Sci.*, vol. 41, no. 4, pp. 517–530, 1996.

[6] W. Wagner, G. Blöschl, P. Pampaloni, J. C. Calvet, B. Bizzarri, J. P. Wigneron, and Y. Kerr, "Operational readiness of microwave remote sensing of soil moisture for hydrologic applications," *Nordic Hydrol.*, vol. 38, no. 1, pp. 1–20, Jan. 2007.

[7] S. Liang, *Quantitative Remote Sensing of Land Surfaces*. New York, USA: Wiley, 2004.

[8] C. Mätzler and A. Standley, "Technical note: Relief effects for passive microwave remote sensing," *Int. J. Remote Sens.*, vol. 21, no. 12, pp. 2403–2412, Dec. 2000.

[9] K. Gwangseob and P. Barros Ana, "Space-time characterization of soil moisture from passive microwave remotely sensed imagery and ancillary data," *Remote Sens. Environ.*, vol. 81, nos. 2–3, pp. 393–403, Aug. 2002.

[10] Y. Kerr, F. Secherre, and J. Lastent, "SMOS: Analysis of perturbing effect cover land surfaces," in *Proc. IEEE Int. Geosci. Remote Sens.*, Jul. 2003, pp. 908–910.

[11] L. Pulvirenti, N. Pierdicca, and F. S. Marzano, "Prediction of the error induced by topography in satellite microwave radiometric observations," *IEEE Trans. Geosci. Remote Sens.*, vol. 99, no. 4, pp. 1–9, Sep. 2011.

[12] K. Y. Kondratyev and M. P. Manolova, "The radiation balance on slopes," *Solar Energy*, vol. 4, no. 1, pp. 14–19, Jan. 1960.

[13] D. M. Gates and R. Janke, "The energy environment of the alpine tundra," *Oecol. Plant.*, vol. 1, pp. 39–62, Feb. 1966.

[14] B. J. Garnier and A. Ohmura, "A method of calculating the direct shortwave radiation income on slopes," *J. Appl. Meteorol.*, vol. 7, no. 5, pp. 796–800, Oct. 1968.

[15] C. R. Duguay, "Radiation modeling in mountainous terrain review and status," *Mountain Res. Develop.*, vol. 13, no. 4, pp. 339–357, Nov. 1993.

[16] N. Pierdicca, L. Pulvirenti, and F. S. Marzano, "Simulating topographic effects on spaceborne radiometric observations between L and X frequency bands," *IEEE Trans. Geosci. Remote Sens.*, vol. 48, no. 1, pp. 273–282, Jan. 2010.

[17] L. Pulvirenti, N. Pierdicca, and F. S. Marzano, "Topographic effects on the surface emissivity of a mountainous area observed by a spaceborne microwave radiometer," *Sensors*, vol. 8, no. 3, pp. 1409–1474, Mar. 2008.

[18] A. N. Flores, V. Y. Ivanov, D. Entekhabi, and R. L. Bras, "Impact of hillslope-scale organization of topography, soil moisture, soil temperature, and vegetation on modeling surface microwave radiation emission," *IEEE Trans. Geosci. Remote Sens.*, vol. 47, no. 8, pp. 2557–2571, Aug. 2009.

[19] A. Mialon, L. Core, Y. H. Kerr, F. Sécherre, and J. P. Wigneron, "Flagging the topographic impact on the SMOS signal," *IEEE Trans. Geosci. Remote Sens.*, vol. 46, no. 3, pp. 689–694, Mar. 2008.

[20] C. Utku and D. M. Le Vine, "A model for prediction of the impact of topography on microwave emission," *IEEE Trans. Geosci. Remote Sens.*, vol. 49, no. 1, pp. 395–405, Jan. 2011.

[21] I. Völksch, M. Schwank, and C. Mätzler, "L-band reflectivity of a furrowed soil surface," *IEEE Trans. Geosci. Remote Sens.*, vol. 49, no. 6, pp. 1957–1966, Jun. 2011.

[22] A. Monerris, P. Benedicto, M. Vall-llossera, A. Camps, E. Santanach, M. Piles, and R. Prehn, "Assessment of the topography impact on microwave radiometry at L-band," *J. Geophys. Res.*, vol. 113, no. B12, pp. 1–9, Dec. 2008.

[23] Y. Ma, J. Li, X. Li, X. Tang, Y. Liang, S. Huang, B. Wang, H. Liu, and X. Yang, "Phosphorus accumulation and depletion in soils in wheat-maize cropping systems: Modeling and validation," *Field Crops Res.*, vol. 110, no. 3, pp. 207–212, Feb. 2009.

[24] H. Han, "Analysis of geomorphologic features of the Tibetan plateau based on SRTM-DEM," Ph.D. dissertation, College Earth Environ. Sci., Lanzhou Univ., Lanzhou, China, 2009, pp. 40–41.

[25] T. Zhao, L. Zhang, L. Jiang, S. Zhao, L. Chai, and R. Jin, "A new soil freeze/thaw discriminate algorithm using AMSR-E passive microwave imagery," *Hydrol. Process.*, vol. 25, no. 11, pp. 1704–1716. May 2011.

[26] L. A. Jones, C. R. Ferguson, J. S. Kimball, K. Zhang, S. K. Chan, and K. C. McDonald, "Satellite microwave remote sensing of daily land surface air temperature minima and maxima from AMSR-E," *IEEE J. Sel. Topics Appl. Earth Observat. Remote Sens.*, vol. 3, no. 1, pp. 111–123, Mar. 2010.

[27] E. G. Njoku, P. Ashcroft, T. K. Chan, and L. Li, "Global survey and statistics of radio-frequency interference in AMSR-E land observations," *IEEE Trans. Geosci. Remote Sens.*, vol. 43, no. 5, pp. 938–947, May 2005.

[28] C. Palm, P. Sanchez, S. Ahamed, and A. Awiti, "Soils: A contemporary perspective," *Annu. Rev. Environ. Resour.*, vol. 32, pp. 99–129, Nov. 2007.
[29] M. Kenneth. (2005). *The Community Noah Land-Surface Model (LSM), User's Guide Public Release Version 2.7.1* [Online]. Available FTP: ftp.emc.ncep.noaa.gov/mmb/gcp/ldas/noahlsm/ver_2.7.1
[30] T. G. Farr, P. A. Rosen, E. Caro, R. Crippen, R. Duren, S. Hensley, M. Kobrick, M. Paller, E. Rodriguez, L. Roth, D. Seal, S. Shaffer, J. Shimada, J. Umland, M. Werner, M. Oskin, D. Burbank, and D. Alsdorf, "The shuttle radar topography mission," *Rev. Geophys.*, vol. 45, no. 2, pp. 1–33, Jun. 2007.
[31] R. Latifovic and I. Olthof, "Accuracy assessment using sub-pixel fractional error matrices of global land cover products derived from satellite data," *Remote Sens. Environ.*, vol. 90, no. 2, pp. 153–165, Mar. 2004.
[32] G. Tang, F. Li, and X. Liu, *Digital Elevation Model*, Beijing, China: Science Press, 2009, pp. 48–52.
[33] J. Shi, L. M. Jiang, and L. X. Zhang, "A parameterized multi-frequency-polarization surface emission model," *J. Remote Sens.*, vol. 10, no. 4, pp. 502–514, Dec. 2005.
[34] J. Shi, L. Jiang, L. Zhang, J. P. Wigneron, A. Chanzy, and T. J. Jackson, "Physically based estimation of bare-surface soil moisture with the passive radiometers," *IEEE Trans. Geosci. Remote Sens.*, vol. 44, no. 11, pp. 3145–3153, Nov. 2006.
[35] M. J. Sandells, I. J. Davenport, and R. J. Gurney, "Passive L-band microwave soil moisture retrieval error arising from topography in otherwise uniform scenes," *Adv. Water Resour.*, vol. 31, no. 11, pp. 1433–1443, Nov. 2008.

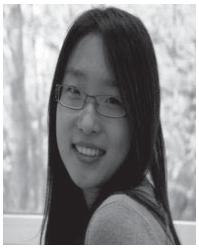

Xinxin Li (M'09) born on September 18, 1985. She received the Bachelor's degree in science from the School of Urban and Environmental Science, Northeast Normal University, Changchun, China, and the Master's and Ph.D. degrees in study program from the School of Geography and Remote Sensing Science, Beijing Normal University, Beijing, China, and the Joint Ph.D. degree from the Institute for Bio- and Geoscience IBG-3, Forschungszentrum Jülich, Jülich, Germany, in 2004, 2008, and 2012, respectively. She is currently studying on passive microwave remote sensing with Beijing Normal University in her last year for a PhD degree.

She has been working on microwave radiative transfer modeling, hydrology, mountain ecology, and climate change.

Dr. Li is a member of the American Geophysical Union, European Geosciences Union.

Lixin Zhang (M'08) received the B.A. degree from the University of Lanzhou, Lanzhou, China, and the M.A. and Ph.D. degrees in geography from the Institute of Glaciology and Geocryology, Lanzhou, in 1988, 1991, and 2000, respectively.

He joined the Research Center for Remote Sensing and GIS, Beijing Normal University, Beijing, China, as a Professor. His current research interests include physical properties of frozen soil, and inversion algorithms or criteria for monitoring physical parameters of soil from remote sensing data.

Lutz Weihermüller received the Diploma degree in geography from University Bremen, Bremen, Germany, and the Ph.D. degree in numerical modelling from the University Bonn, Bonn, Germany, in 2005.

He is currently a Senior Scientist with the Forschungszentrum Jülich, Jülich, Germany. Additionally, he is involved in research on different hydrogeophysical and remote sensing methods such as radar and radiometry for soil water monitoring. His current research interests include the numerical modelling of water, solute, and gas transport in the unsaturated zone and parameter estimation for various applications.

Dr. Weihermüller is a member of the American Geophysical Union, European Geosciences Union, and Soil Science Society of America.

Lingmei Jiang (AM'09) was born in Zhejiang, China, on October 31, 1978. She received the B.S. degree in agricultural meteorology from the Nanjing Institute of Meteorology, Nanjing, China, in 2000, and the Ph.D. degree in geography from Beijing Normal University, Beijing, China, in 2005.

Her current research interests include microwave remote sensing and modeling and retrieval of snow and soil properties.

Harry Vereecken (M'–) received the Degree in agricultural engineering and the Ph.D. degree in agricultural sciences from the Katholieke Universiteit Leuven, Leuven, Belgium, in 1982 and 1988, respectively. His Ph.D. thesis was on the development of pedotransfer functions to estimate soil hydraulic properties.

He was a Research Assistant on modeling nitrogen and water fluxes in soils and groundwater from 1988 to 1990. He was a Researcher with the Institute of Petroleum and Organic Geochemistry, Forschungszentrum Jülich, Jülich, Germany, from 1990 to 1992, where from 1992 to 2000, he became the Head of the Division behavior of pollutants in geological systems. He was the Director of the Institute of Agrosphere in 2000. His current research interests include modeling of flow and transport processes in soils and hydrogeophysics.